Available online at www.sciencedirect.com
SCIENCE DIRECT
International Journal of Heat and Mass Transfer 49 (2006) 919–938
International Journal of HEAT and MASS TRANSFER
www.elsevier.com/locate/ijhmt

Numerical approach to hole shape effect on film cooling effectiveness over flat plate including internal impingement cooling chamber

Jr-Ming Miao [a,*], Chen-Yuan Wu [b]

[a] Department of Mechanical Engineering, Chung Cheng Institute of Technology, National Defense University, 335 Taoyuan, Taiwan, ROC
[b] Graduate School of Defense Science Studies, Chung Cheng Institute of Technology, National Defense University, 335 Taoyuan, Taiwan, ROC

Received 29 November 2004; received in revised form 30 July 2005
Available online 16 November 2005

Abstract

Numerical approach have been conducted on a flat, three-dimensional discrete-hole film cooling geometries that included the main-flow, injection tubes, impingement chamber, and supply plenum regions. The effects of blowing ratio and hole's shape on the distributions of flow field and adiabatic film cooling effectiveness over a flat plate collocated with two rows of injection holes in staggered-hole arrangement were studied. The blowing ratio was varied from 0.3 to 1.5, while the density ratio of the coolant to mainstream is kept at 1.14. The geometrical shapes of the vent of the cooling holes are cylindrical round, simple angle (CYSA), forward-diffused, simple angle (FDSA) and laterally diffused, simple angle (LDSA). Diameter of different shape of cooling holes in entrance surface are 5.0 mm and the injection angle with the main stream in streamwise and spanwise are 35° and 0° respectively. Ratio of the length of the cooling holes and the diameter in the entrance surface is 3.5. The distance between the holes in the same row as well as to the next row is three times the diameter of hole in the entrance surface.

The governing equation is the fully elliptic, three-dimensional Reynolds-averaged Navier–Stokes equations. The mesh used in the finite-volume numerical computation is the multi-block and body-fitted grid system. The simulated streamwise distribution of spanwise-averaged film cooling effectiveness exhibited that low Reynolds number k–ε model can give close fit to the experimental data of the previous investigators. Present study reveals that (1) the geometrical shape of the cooling holes has great effect on the adiabatic film cooling efficiency especially in the area near to the cooling holes. (2) The thermal-flow field over the surface of the film-cooled tested plate dominated by strength of the counter-rotating vortex pairs (CRVP) that generated by the interaction of individual cooling jet and the mainstream. For LDSA shape of hole, the CRVP are almost disappeared. The LDSA shape has shown a highest value in distribution of spanwise-averaged film cooling effectiveness when the blowing ratio increased to 1.5. It is due to the structure of the LDSA is capable of reducing the momentum of the cooling flow at the vent of the cooling holes, thus reduced the penetration of the main stream. (3) The structure of the LDSA can also increase the lateral spread of the cooling flow, thus improves the spanwise-averaged film cooled efficiency.

Keywords: Computational fluid dynamic; Impingement cooling; Film cooling; Lateral diffused hole; Turbines

1. Introduction

In pursuit of higher thrust and heat efficiency of a turbo engine, the proper and effective protection for the turbine blades working under a high temperature and pressure environment has been an inevitable task. External film cooling was widely used to reduce the heat stress. The working principle of the film cooling is to let the lower temperature passes through the holes on the surface of the blades, in order to form an air film with lower temperature between the surface of the blade and the main stream to

* Corresponding author. Tel.: +886 3 3893475; fax: +886 3 3895924.
E-mail address: jmmiao@ccit.edu.tw (J.-M. Miao).

0017-9310/$ - see front matter © 2005 Elsevier Ltd. All rights reserved.
doi:10.1016/j.ijheatmasstransfer.2005.09.015

Nomenclature

B	body force, kg
BR	blowing ratio
D_i	diameter of the impinging hole, m
D_c	diameter of the film cooling hole, m
H	total enthalpy
h	static enthalpy
k	kinetic turbulence
L	thickness of the sample
p	pressure, Pa
S	source
T_{aw}	adiabatic temperature of the wall, K
T_c	temperature of the cooling stream, K
T_m	temperature of the main stream, K
t	time, s
$\vec{U}$	velocity vector of x, y, z direction
U, V, W	velocity of x, y, z direction, m/s
u_c	velocity of the cooling stream, m/s
u_m	velocity of the mainstream, m/s
x, y, z	coordinates

Greek symbols

Γ	diffusion coefficient
ε	dissipation rate
η	adiabatic film cooling efficiency
ρ_c	density of the cooing stream, kg/m^3
ρ_m	density of the main stream, kg/m^3
σ	stress tensor, N/m^2
Φ	dependent variable

protect the turbine blade. Many factors are involved in the film cooling process. Some of the main factors are the curve of the blade surface, the strength of the turbulence in the main stream, compressibility of the stream, unsteady characteristics of the stream, size of the cooling holes, shape and the location of the holes, angle between the cooling jet and the main stream, and the path of the cooling flow. Moreover, the momentum ratio (blowing ratio) and the density ratio between the cooling jet and the main stream also play an important part in the film cooling performance. Fig. 1 [1] shows the diagram of the internal cooling system for a turbine blade. The cooling stream flow will eject through the impinging holes into the impinging chamber when it enters the blade and achieves the cooling purpose by flowing through the film cooling holes to the surface of the blade.

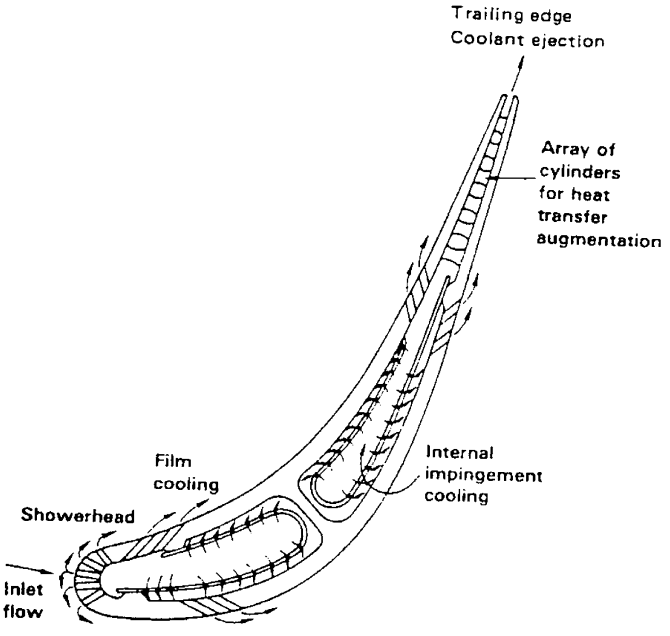

Fig. 1. Schematic of cooling arrangement in a turbine blade [1].

Film cooling and impingement cooling are two of the main studies in this topic. Some of the film cooling flat plate studies with cylindrical holes are carried out by Ammari et al. [2], Goldstein et al. [3] and Baldauf et al. [4,5]. While Loftus and Jones [6] as well as Ligrani et al. [7] has applied various working fluid to the cooling flow in order to study the film cooling efficiency under different density ratio. The above studies are mainly experimental measurement, thus all results data are only the local and spanwise-averaged heat transfer coefficient, or the film cooling effectiveness distributed on the surface of the test sample. It is obvious that the temperature topology on the surface of test sample is directly response to the transport phenomena resulting from interaction of coolant jets with the cross-mainstream. The angle orientation and length of hole will affect the structure of the flow field developing within the passage of cooling pipe. Cho and Goldstein [8] has used the naphthalene sublimation mass transfer technique to investigate the characteristic of the heat transfer within the film cooling holes, where the major study is the blowing ratio effect. They have concluded in the paper that the flow field within the cooling pipe can be separated into four part: the separated/back flow area near the cooling hole entrance, the re-attachment area, developing area and the area at the tail end downstream near the cooling hole which affected by the main stream. They have discovered the structure and cooling flow above area have great relationship to the blowing ratio, and the film cooling effects are also affected by the structure of the flow field developed in the cooling pipe.

As for the authors' knowledge, one of the systematic researches that concerned about the film-cooled problems with three-dimensional computational approach was accomplished by Leylek and Zerkle [9] who used a flat plate model with one row of five cylindrical holes to analyze the effects of blowing ratio and hole length-to-diameter ratio

on film cooling performance. They have adopted the wall function of standard k–ε turbulent model to treat the near-wall quantity of turbulent profile. In spite of flow passage of mainstream, the computational domain also included the cooling flow at the supplying plenum, and coolant pipes. The flow structure of the velocity vectors on different streamwise planes normal to cross-stream is very complicated and they concluded that there is also a pair of counter-rotating vortex that dominated the interaction of individual coolant jet and cross-mainstream. The local jetting effect occurred within the coolant pipes will significantly affect the distributions of film cooling effectiveness on the near-hole field. Later Hyams and Leylek [10] have focused on the detailed analysis in physics of film cooling process for five various kinds of shaped, streamwise-injected, inclined jets. This study suggested that the crucial flow mechanisms downstream of discrete-cooling hole could be clarified from a vorticity point of view. It can be observed from their results that the shape of the cooling holes has great effect to the downstream film cooling performance.

Bell et al. [11] also study the effects of the shape and angle orientation of the film cooling holes, such as: CYSA, LDSA, LDCA, FDSA and FDCA on the film cooling effectiveness by using experimental method. They have discovered that LDCA has the best film cooling performance, followed by FDCA over the range of blowing ratios from 0.5 to 2.0. This is caused by the film diffusion from expanded holes shape. This consideration in lateral spreading of injection can reduce the exit momentum of the cooling flow and increase the diffusion effect at the lateral direction. Therefore, less jet penetration effect and lower velocity gradient are expected. Gritsch et al. [12] has used infrared thermal-photographic system to analyze the heat transfer coefficients in the near-hole region of various shapes of the cooling hole with a flat plate model. The results show that fan type design with laterally expanded hole will have a lower heat transfer coefficient distribution when the blowing ratio is higher.

Jung and Lee [13], in the mean time, also analyzed the compound angle effect and discovered that increasing the compound angle enhances the spanwise-averaged film cooling effectiveness. The cooling effect produced by positioning with larger lateral orientation angle is more conspicuous under high blowing ratio. Since the forward- or lateral-expanded hole can be more effectively avoiding the lift-off phenomena under high blowing ratio than cylindrical round hole, Yu et al. [14] has integrated the forward-expanded hole and lateral-expanded hole into a new distributed hole and discovered that it can both decrease the heat transfer coefficient and greatly increase the film cooling effectiveness especially in the area where is closed to the cooling holes.

In order to improve the heat transfer in the advance turbine blade, the cooling stream is being cooled twice where the cooling stream will complete the internal cooling inside the impingement chamber before blowing out from the cooling pipes beneath the surfaces of the blade to perform the external film cooling. Behbahani and Goldstein [15], Huang et al. [16] and Azad et al. [17] have literatures on the study of heat transfer of the impingement cooling in the turbine blade. Downs and James [18] has suggested that the factors that affect the heat and mass transfer of the impingement cooling are: geometrical structure, temperature, the interaction between the cooling stream and the lateral stream, strength of the turbulence and the structure of the hole of the cooling jet. Viskanta [19] also pointed out that the factors that affect the performance of the impingement cooling are: interaction between the jet and wall, separation distance, pitch between the adjacent jets, diameter of the hole of the jet, characteristic of the main stream and the surface topology of target plate. All the above studies focus on the heat transfer of a physical flat plate impingement cooling with several effusion holes. Cho et al. [20] have studied this issue and discovered that when the distance between the impingement pipe plate and the target plate is smaller, the value of local distribution of the heat/mass transfer at the contact surface of the target plate would be higher.

One of the major conclusions in a review article of Schiele and Wittig [21] is that there is very close relationship between the supply type of the cooling flow and the film cooling performance due to the variation of discharge coefficient and local jetting effect within coolant pipes. However, most of the studies nowadays still focus in experimental simulations, and there is no literature so far has systematically investigated both the internal impingement cooling and external film cooling together with numerical approach. Therefore, the main features of this study are: (1) Realistic, dual function of internal impingement cooling and external film cooling geometries have been used that included the mainstream, two rows of staggered injection coolant pipes, impingement pipe plate, and the supply plenum regions, (2) the effects of hole's shape and blowing ratio on film cooling effectiveness are studied and (3) The underlying reasons for these effects have been discussed using velocity contours and velocity vectors at centerline of each of coolant pipes and at several cross-stream planes downstream of holes.

2. Numerical model

Fig. 2 shows the numerical model of the impingement cooling and film cooling flat plate used in this paper. The paths can be separated into the rectangle shaped path for the upper mainstream and the path for the lower cooling stream from the two rows of staggered cooling holes, while an impingement region is set in the path of the cooling stream. A three-dimensional computational domain include the rectangle mainstream, the collocated cooling holes and the supplying path of the cooling stream was constructed. While an impingement chamber with array of holes is set up in the cooling flow supplying path located beneath twice the diameter of the cooling hole from the

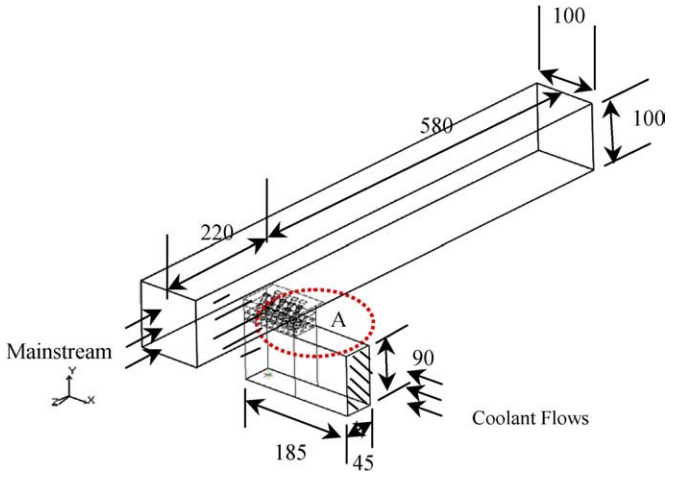

Fig. 2. The geometry of the film-cooled flat plate with internal impingement chamber, unit: mm.

entrance of the cooling holes to simulate the internal impingement cooling effect. A film-cooled flat plate model without internal impingement hole pipe is also constructed. The size of the path of the mainstream is 100 mm × 100 mm × 800 mm (width × height × long), while the size of the path of the cooling stream is 45 mm × 90 mm × 185 mm (width × height × long). The area with an "A" mark in Fig. 2 included the impingement cooling holes array, impingement chamber and the two rows of film cooling holes array.

The close view of the area presented in Fig. 3. There are two rows of film cooling holes where the first row from the upper stream has five holes arranged in equal distance, and the second row will have four holes. The two rows interlaced with each other. The streamwise angle between the axis of each cooling hole and the main stream is 35°, and the spanwise angle between the axis and the cross-flow direction is 0°. The diameter of the entrance of the cooling holes (D_c) is 5 mm, where the ratio between the diameter of the entrance of the cooling hole and the length of the cooing hole is 3.5, and is 3.0 with the distance to the center of the next parallel row as well as the longitudinal row. Where the impingement holes arrays are nine holes in three row or eight holes in two rows, with a total of 43 impinging holes, where the nine holes are arranged interlace with the eight holes. The diameter (D_i) and the length of the impingement holes are 5 mm and 10 mm respectively, and the distance between holes is $2 \times D_i$, while the impingement distance (distance from the exit of the impingement hole and entrance of the cooling hole) is also $2 \times D_i$.

We have studied three kinds of geometrical shapes of hole in this paper, which are

(1) Cylindrical round, simple angle hole (CYSA), as shown in Fig. 4(a).
(2) Forward-diffused, simple angle hole (FDSA), where a taper angle of 15° is applied to the trail edge of exit, as shown in Fig. 4(b).

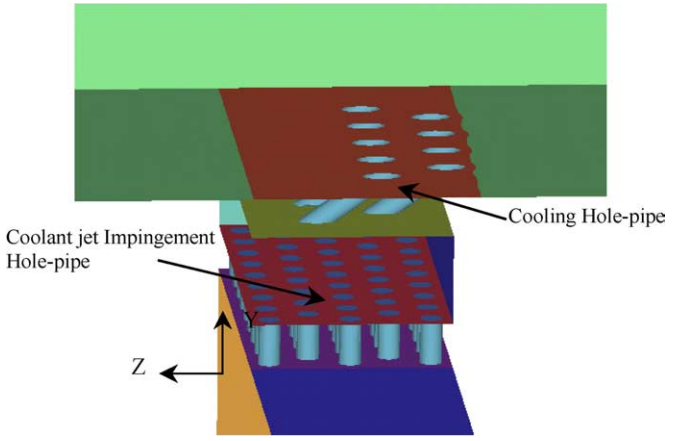

Fig. 3. The close view of two rows of cooling tubes and internal impingement regions marked as A.

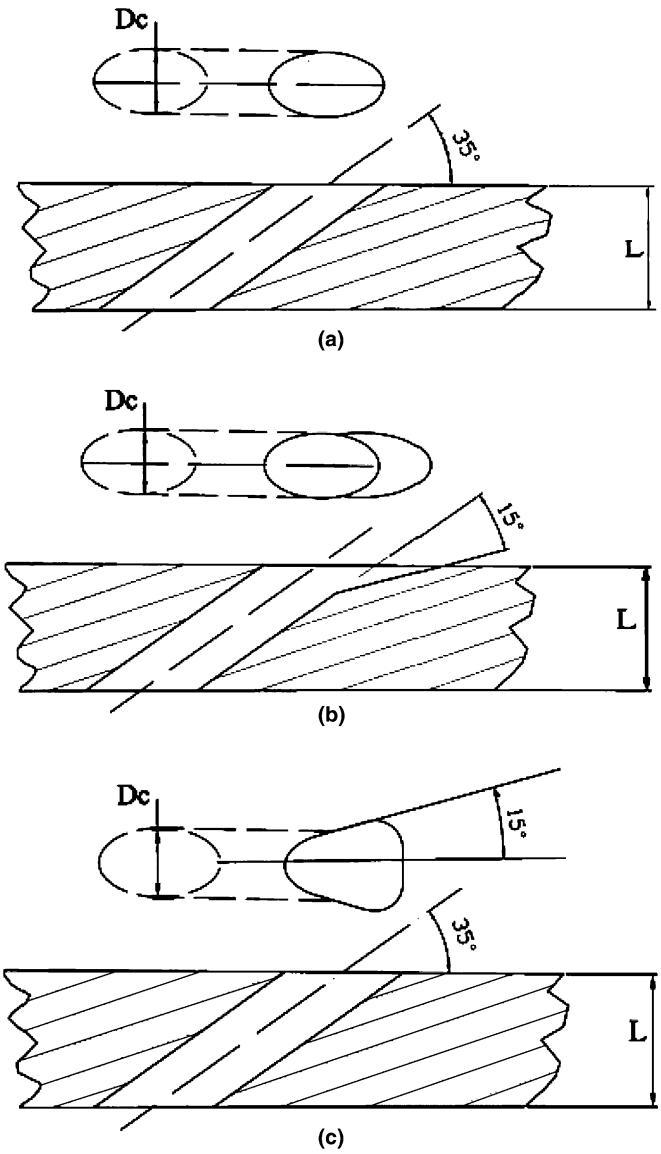

Fig. 4. Schematic geometry of film cooling hole: (a) CYSA, (b) FDSA and (c) LDSA.

(3) Lateral diffused, simple angle hole (LDSA), where a taper angle of 15° are applied to both lateral sides of exit, as shown in Fig. 4(c).

3. Grid system

Many studies, for examples of Cho and Goldstein [8], Schiele and Wittig [21], have stated that the performance of the film cooling for the surface of the sample is highly related to the flow physics of distinct jet within the cooling pipe and the feeding path of the supplying cooling stream. In order to present the characteristic of the heat flow field by the dual effects—internal impingement cooling and the external film cooling, we have included the supplying area of cooling stream, impingement pipes plate, impingement chamber, cooling pipe array and the main stream as the computational areas.

Because of the geometrical complexity of impingement cooling/film cooling problems, the physical model and structured multi-block grid system constructed by the HEXA module in software package ICEM/CFD. This software allows generating separately grids for the different parts of the flow domain using a suitable grid generator. In present study, the grid system for the parts of the mainstream and cooling supplying plenum are H-type grid system, while the round impingement pipe array and two rows of round-like cooling pipes will used the O-type grid system to increase the orthogonality of the mesh. Grid sensitivity studies show that with the low Reynolds number k–ε turbulence model using wall function, grid-independent results can be obtained with $87\times47\times117$ nodes in x-, y- and z-directions of mainstream duct. The cells were considered refined in the near-wall regions of tested plate and in the vicinity of the injection hole. The y^+ value in the first cell adjacent to the sample walls was set always below 1 with respect to the criteria required for the individual near-wall treatment. Fig. 5 shows the grid feature of the exit of the LDSA cooling holes and region near the surface of the sample plate. The multi-block topology and high quantity of grid system can be clearly observed.

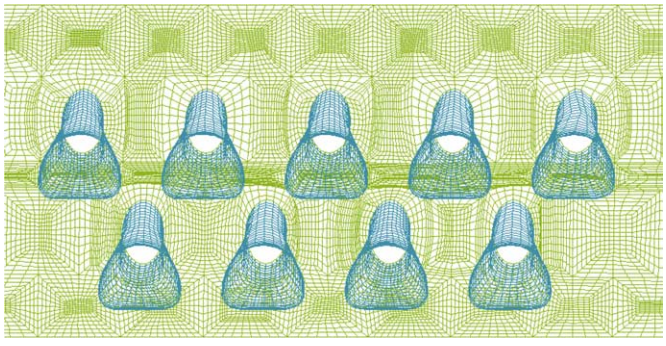

Fig. 5. The grid features on both of inner surface and the surface perpendicular to the axial of LDSA cooling hole.

4. Governing equations

The numerical solver is a package of software, CFX-4.4, which was developed by AEA to solve the conservation governing equations, i.e. three-dimensional Reynolds-averaged Navier–Stokes equations. While the scalar advection–diffusion in conservative form is written as

$$\frac{\partial}{\partial t}(\rho\Phi)+\nabla\cdot(\rho\vec{U}\Phi-\Gamma\nabla\Phi)=S \tag{1}$$

The continuous equation, momentum equation, and the energy equation can be expressed as below:

Continuous equation:

$$\frac{\partial\rho}{\partial t}+\nabla\cdot(\rho\vec{U})=0 \tag{2}$$

Momentum equation:

$$\partial\rho\vec{U}/\partial t+\nabla\cdot(\rho\vec{U}\otimes\vec{U})=B+\nabla\cdot\sigma \tag{3}$$

where σ is the stress tensor, stated as below:

$$\sigma=-p\delta+\left(\zeta-\frac{2}{3}\mu\right)\nabla\cdot\vec{U}\delta+\mu(\nabla\vec{U}+(\nabla\vec{U})^{\mathrm{T}}) \tag{4}$$

Energy equation:

$$\partial\rho H/\partial t+\nabla\cdot(\rho\vec{U}H)-\nabla\cdot(\lambda\nabla T)=\partial p/\partial t \tag{5}$$

where H is total enthalpy defined as below:

$$H=h+(1/2)\vec{U}^2 \tag{6}$$

where h is static enthalpy, ρ is the density of the fluid, $\vec{U}=(U,V,W)$ is the velocity, P is the pressure, T is the temperature, t is the time, B is the body force, μ is the dynamic viscosity, and ζ is the bulk viscosity.

It should be noted that this study would have to deal with the heat buoyancy effect under different temperature between the mainstream and the cooling stream. The Boussinesq's approximation on the density of fluid is applied and stated below:

$$\rho=\rho_0(1-\beta(T-T_0)) \tag{7}$$

where ρ_0 and T_0 are reference density and temperature respectively, while β is the thermal expansion coefficient.

Numerically, the transport equation will be discretized with the conservative finite volume method. The advection term will be approximated with the second order hybrid difference scheme, while all others will use the central-difference scheme. The coupler between the velocity and the pressure will use the SIMPLEC algorithm and the algebraic multi-grid method will be adapted to speedup the converging process. A detailed description about the mathematics of numerical method is referred in User manual of CFX4.4.

5. Turbulence model

Since the characteristic of the thermal-flow field downstream of cooling holes is strongly affected by the interaction between the cross-mainstream and the two rows of

inclined cooling jet, the accuracy of simulated results by different turbulence models should be validated in advance. Present study started with a simpler model in Ai et al. [22], and used the one row of round discrete-hole flat plate model from their experiment for the numerical simulation. Runs with low Reynolds number k–ε are conducted for comparison with the experimental results. The complete mathematical theory and the associated boundary conditions for solving of turbulent kinetic energy and rate of dissipation energy in low Reynolds number turbulence model could be referenced to [23].

6. Boundary conditions and study matrix

The normal speed of the mainstream is uniform set as 10 m/s, therefore the corresponding Reynolds numbers with the diameter of the cooling holes at entrance surface as the characteristic length is 3400. For simulation of film cooling effect, the temperature of the mainstream maintains as 333 K, and temperature of the cooling stream is lower as 293 K. In addition, the turbulence intensity and dissipation length at the inlet boundary of mainstream are 4% and 15% of hydrodynamic diameter, respectively. The same turbulence intensity is set at inlet boundary of coolant but the value of dissipation length is changed to D_c value. The mass flow rate of coolant could be determined by the tested flow parameter, which is blowing ratio (BR) defined as below:

$$\mathrm{BR} = \frac{\rho_c u_c}{\rho_m u_m} \tag{8}$$

where ρ and u are the density and speed respectively, the subscript c and m are the coolant flow and mainstream respectively. The blowing ratios used in this paper are 0.3, 0.6, 0.9, 1.2, and 1.5 with the density ratio of 1.14. The surface boundary condition of the solid walls are all defined to be non-slip and adiabatic. Pressure boundary condition is specified at the exit of mainstream flow passage. The study matrix is listed in Table 1, including of information on applied blowing ratio and shapes of the cooling hole.

In spite of the velocity contours and velocity vectors shown at different cross-planes, the computational results are presented and compared by introducing a non-dimensional parameter-local adiabatic film cooling effectiveness, defined as

Table 1
Study matrix

Numerical model	Blowing ratio	Turbulence model
One row of CYSA [22]	0.5	Low Reynolds k–ε
Two rows of CYSA (without impingement coolant pipe)	0.3, 0.6, 0.9, 1.2, 1.5	Low Reynolds k–ε
Two rows of CYSA	0.3, 0.6, 0.9, 1.2, 1.5	Low Reynolds k–ε
Two rows of FDSA	0.3, 0.6, 0.9, 1.2, 1.5	Low Reynolds k–ε
Two rows of LDSA	0.3, 0.6, 0.9, 1.2, 1.5	Low Reynolds k–ε

$$\eta = \frac{T_{aw} - T_m}{T_c - T_m} \tag{9}$$

where T is the absolute temperature, the subscript aw is the adiabatic wall, c is the cooling stream, and m is the main stream.

7. Results and discussion

7.1. Validation

Since there is a lack of experimental data to validate the computational results when using film-cooled flat plate models with internal impingement cooling chamber, a prior numerical study with a simpler geometrical model was constructed. In literatures, a lot of studies investigated on effects of flow parameters on thermal-flow structure and film cooling performance of one-row of discrete-hole cooling plate to reference. Fig. 6 shows the simulated streamwise distributions of spanwise-averaged film cooling effectiveness with low-Reynolds number k–ε turbulence model and differential Reynolds stress turbulence model as the turbulence enclosure. The blowing ratio is 0.5. The experimental results conducted by Ai et al. [22], Jung and Lee [13] and Nasir et al. [24] are also included for comparison. It should be noted that the present simulated geometrical model and the proper boundary conditions are set as the same as those of Ai et al. [22].

While the simulation is being lightly over-predicted for low-Reynolds number k–ε in regions of $Z/D_c \leqslant 15$ and being lightly under-predicted downstream of $Z/D_c = 15$. The reason can be attributed to the isentropic treatment in Reynolds stress flux of above turbulence model. Generally, the predicted data with low-Reynolds k–ε turbulence model is closely fitted with experimental data. Thus, this study will adopt the low-Reynolds number k–ε turbulence

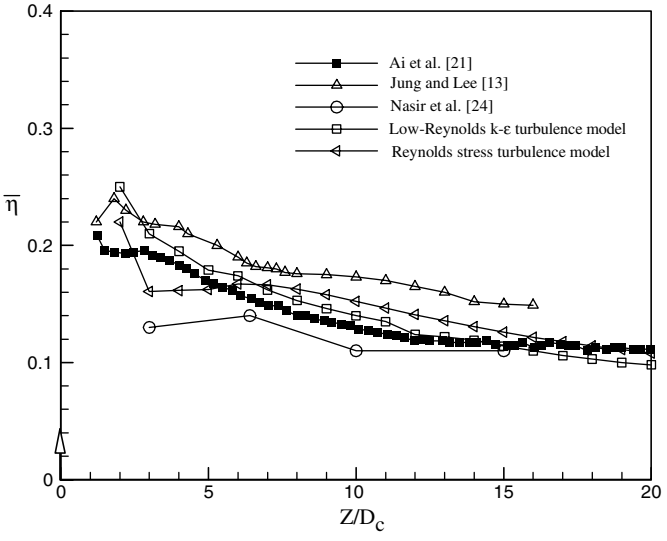

Fig. 6. The distribution of spanwise-averaged adiabatic film cooling effectiveness over flat plate with one row of discrete holes.

model to deal with all the Reynolds stress items in further runs.

7.2. Sensitivity test of the grids system

One of the aims of present study is to set up a complex flow domain for simulation, where the computational areas include the supplying tank for the cooling stream, impinging holes array, impinging chamber, film cooling holes array and the main stream. Three sample grid systems are M1, M2, and M3, where total numbers of grids are 772,068, 966,614, and 1,040,604 respectively. Since the total computational area is very complicated and the main issue considered is the distribution of the film cooling effectiveness for different blowing ratios, the major difference among the three grid systems would be the number of nodes close to intersection regions of coolant pipes and mainstream duct. Moreover, the thickness of the grid system at the first layer of cell above the sample surface is ensured that the y^+ value less than 1. When the blowing ratio is set to 1.2, the distribution curve for the spanwise-averaged adiabatic film cooling effectiveness is compared. Grid sensitivity tests using M2 and M3 grid systems show that the deviation in $\bar{\eta}$ results is within 5% for most portions of tested sample. Considering the CPU time cost and memory requirement for computation; the M2 grid system is selected for all further runs.

7.3. Distribution of the local film cooling efficiency

Fig. 7 shows the top view of the exit of the coolant pipes array, where the main stream is flowing to the right. The cooling holes at the left side are marked as the first row, where the cooling holes at the right side are marked as the second row. The first row contains five cooling holes marked as H1–H5, while the second row have four cooling holes marked as H6–H9. The first and second rows are arranged staggered. The location of the central of the first row of the cooling holes of the main stream is defined as $Z/D_c = 0$, while the location of the central of the second row of the cooling holes of the mainstream is referred as $Z/D_c = 3$. The contours of the local adiabatic film cooling effectiveness for different shapes of cooling holes when the blowing ratio is 0.6, 0.9 and 1.2 respectively are shown in Figs. 8–10. Different shapes of cooling holes will result in a remarkably difference on laterally spreading of higher local adiabatic film cooling effectiveness under same blowing ratio especially at the area near the exit of the cooling stream. The area covered by the cooling stream for all tested three kinds of shapes of hole is larger with increasing of the blowing ratio.

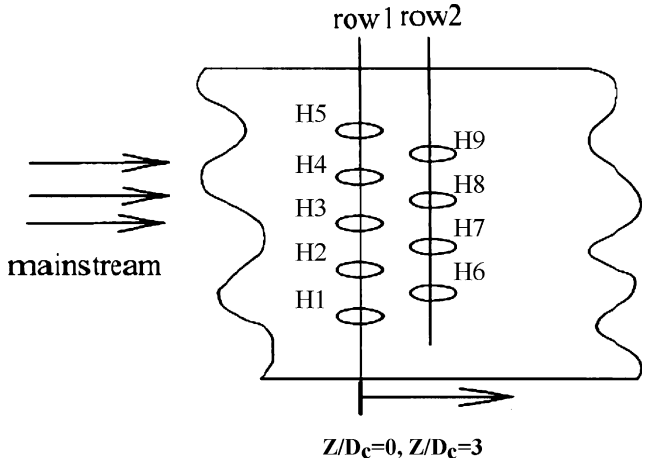

Fig. 7. Top view around cooling holes exit area.

Fig. 8(a)–(c) shows that only downstream regime that next to the exit of the cooling hole has a higher η value. Further downstream, because of the jetting effect within path of cooling pipes and the strong turbulence shear flow structure as meeting with the cross-mainstream, the visible protection region which is relating to the streamwise movement of discrete-hole ejected coolant stream will obviously diminish and present as a triangular-like shrink profile in η distribution. In area of adjacent holes for each row, simulated results displayed that periodic lower η value would cover the mainly section, which indicates that the CYSA structure is not able to provide a cooling effect at the lateral direction. The distributions of η for FDSA cooling holes at various blowing ratio can be seen in Fig. 9(a)–(c). The main difference between Figs. 9 and 8 is the longer distance of high η value distribution at the downstream trailing edge of the FDSA cooling holes at the same blowing ratio. The taper angle of 15° at the trailing edge has successfully reduce the momentum of the cooling stream at the exit of the cooling hole and reduce the penetration effect into the mainstream, thus would provide a better cooling performance at the surface of the sample.

Fig. 10(a)–(c) are the distribution of η value for the LDSA cooling hole structure at various blowing ratios. LDSA cooling hole has a remarkably wider area of surface of the sample that protected by the cooling stream compared to both FDSA and CYSA at the same blowing ratio. This is due to the extended 15° taper angle consideration at both lateral sides of the exit of the cooling hole increases the flow area of the cooling stream, therefore a reducing in momentum ratio for prevention of penetration effect and weakly the strength of shear flow at high blowing ratios. Fig. 10(a)–(c) also shows that a remarkably reduce of low η region between two LDSA cooling holes compared to CYSA and FDSA cooling holes structure due to the lateral flow spreading effect. Generally, the lateral spreading effect of the cooling jet in LDSA has a relatively even cooling protection effect on the surface of the sample.

When the blowing ratio is 1.2, Fig. 11(a)–(c) are the streamwise distributions of the local film cooling effectiveness along the centerline of the first and second row cooling holes for three different kinds of cooling hole structures. The first and second rows of cooling holes of the mainstream are indicated by the hollow and solid arrows respectively on the X-axis, while H1–H5 and H6–H9 (shown in

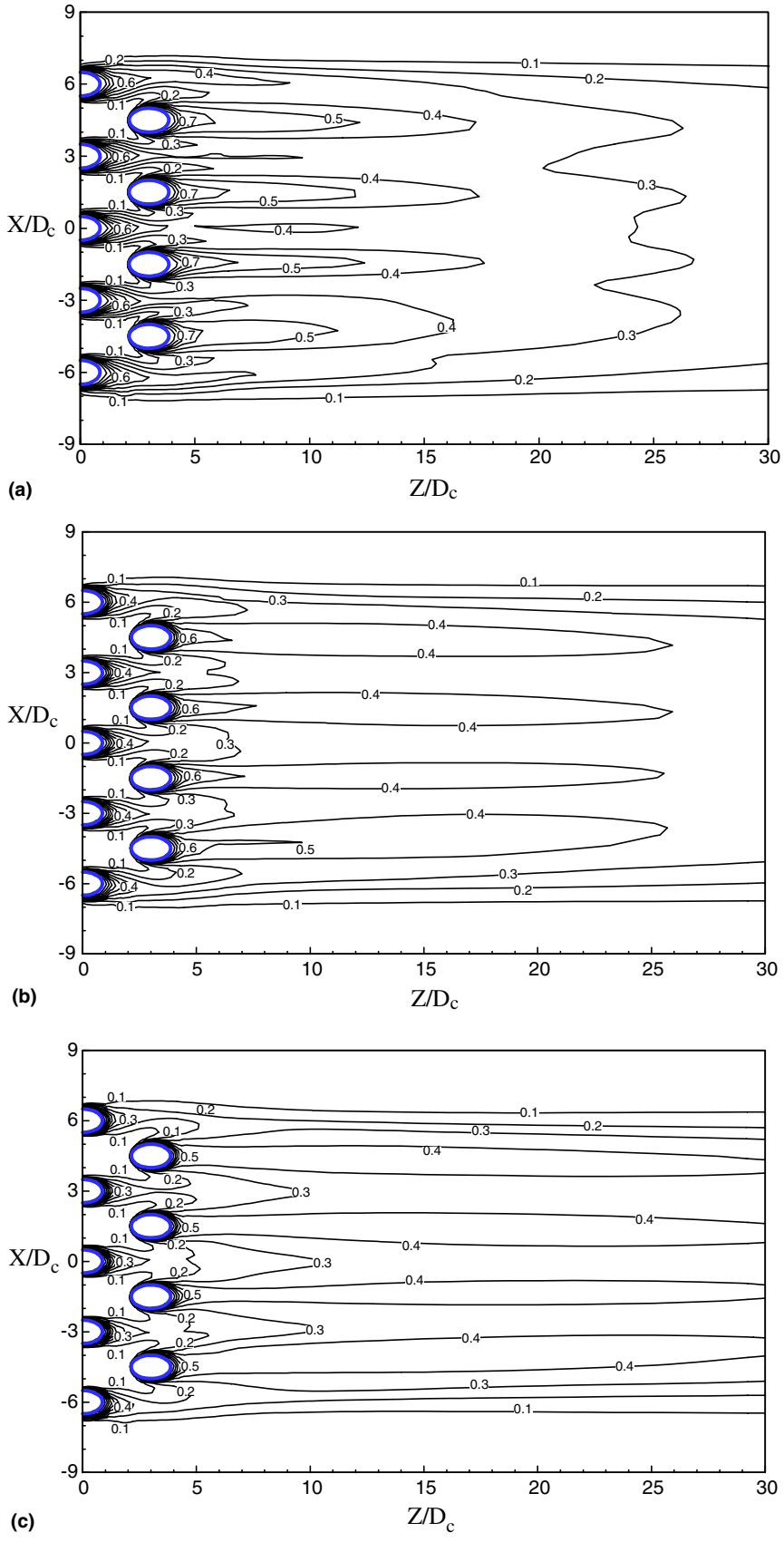

Fig. 8. Contour plots of local film cooling effectiveness for CYSA hole: (a) BR = 0.6; (b) BR = 0.9 and (c) BR = 1.2.

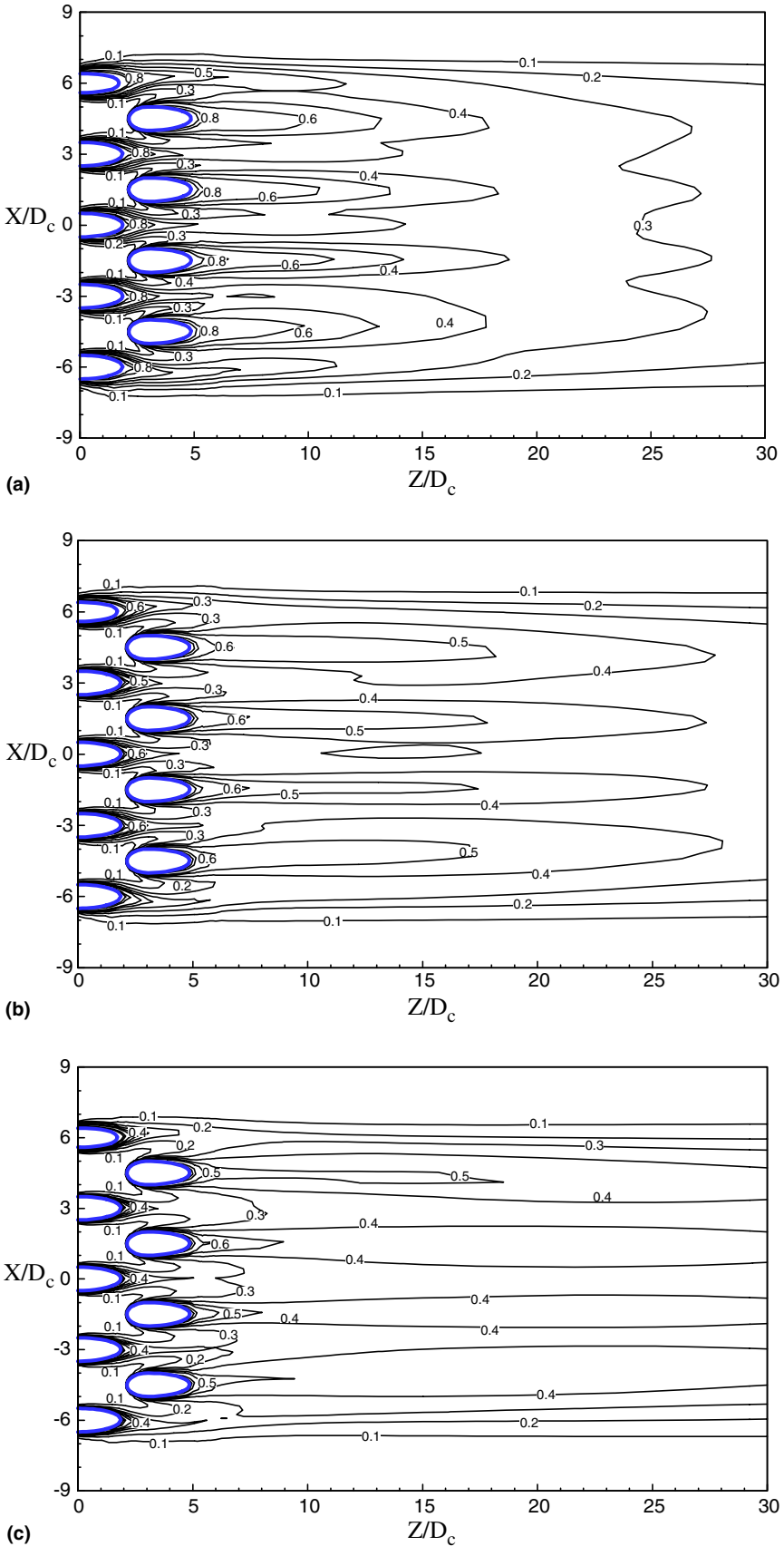

Fig. 9. Contour plots of local film cooling effectiveness for FDSA hole: (a) BR = 0.6; (b) BR = 0.9 and (c) BR = 1.2.

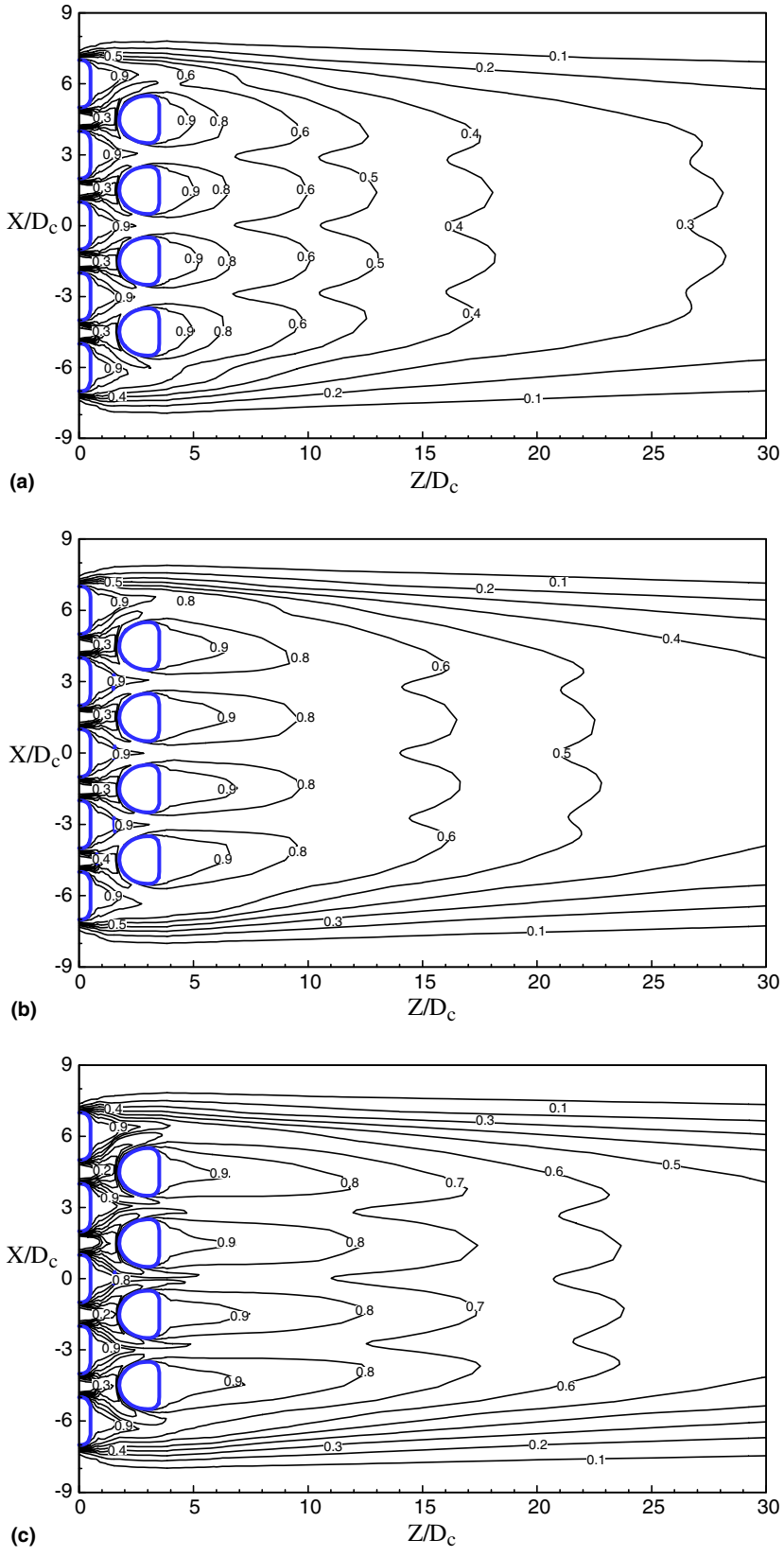

Fig. 10. Contour plots of local film cooling effectiveness for LDSA hole: (a) BR = 0.6; (b) BR = 0.9 and (c) BR = 1.2.

Fig. 7) represent the holes in the first row and second row respectively. Since the cooling stream is induced from the lateral side, through the impingement pipes row into the chamber, and blown out from each cooling holes to per-

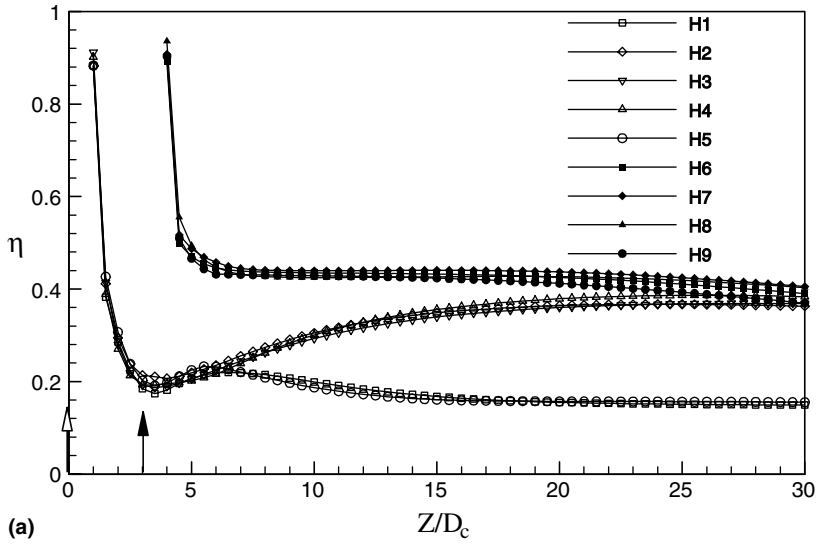

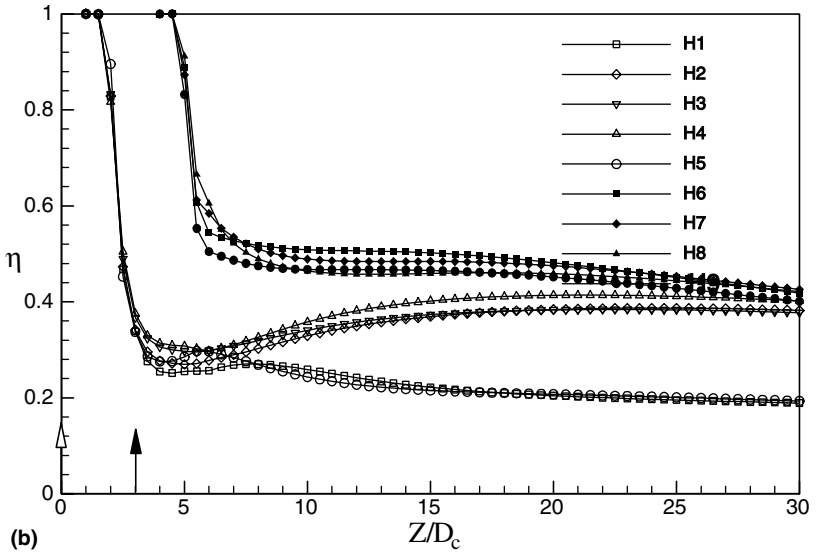

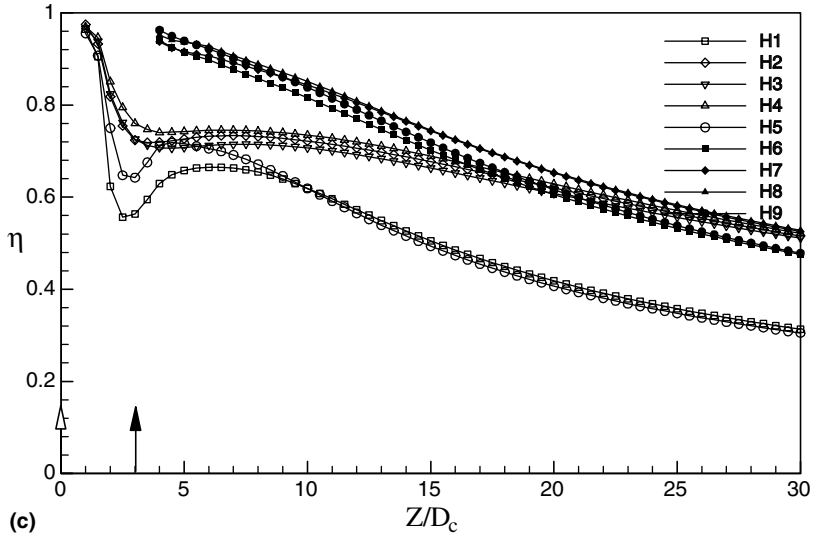

Fig. 11. Distributions of centerline film cooling effectiveness for different shapes of hole at BR = 1.2: (a) CYSA, (b) FDSA and (c)LDSA.

form an interaction between the cooling streams and the mainstream that will cause a slightly un-symmetrical distribution of the local film cooling effectiveness for the cooling holes of the same row, such as H1 and H5, H4 and H9 as well as H7 and H8. Besides, the cooling holes in the first and second rows are arranged interlacing on the sample plate, the cooling jet blow out from H1–H5 will contact with the hot mainstream directly, then a strong convection mechanism will cause the η value decrease rapidly within a very short distance ($0 < Z/D_c < 3$), but level up after that due to the cooling stream ejected from the second row.

Downstream of $Z/D_c = 5$, the local film cooling effectiveness along the streamline is declined gradually for all runs. We discovered that the expanded angle in the trail edge of hole can gradually reduce the degree of penetration of the cooling stream into the main stream by comparing Fig. 11(a) and (b), thus enable the area near the cooling holes can maintain a relatively higher η value. While in LDSA (Fig. 11(c)), since the cooling jets from cooling holes of the first and second rows have a lateral covering capability, the η value along the stream line from H1–H5 is the highest and reduce slowest among the three kinds of cooling holes. Same results can be observed for other blowing ratios.

7.4. Blowing ratio effect

Fig. 12(a)–(c) are the lateral distributions of the curve of the local η value at different streamwise locations of Z/D_c for the CYSA type cooling holes under the blowing ratio of 0.6, 0.9 and 1.2, respectively. The coordinate of the cooling holes is in lateral axis where the hollow arrows represent the first row of cooling holes and the solid arrows represent the second. Similarly, the hollow symbol in the curve of the distribution of local η represent the results between the first row and the second row of cooling holes, while the solid symbols represent the results of downstream of the second row of cooling holes. The routine peak value of the η distribution has highly reflected the trajectory of each coolant jet.

First, observing the curve at the location of $Z/D_c = 1.5$ in Fig. 12(a), where $Z/D_c = 1.5$ indicates the central location between the axis of the first row, and second row of cooling holes. The trend of the curve exhibits that the η value between two cooling holes is almost under 0.1, which indicates that the cooling stream is not able to provide any laterally cooling effect to any of these areas. At $Z/D_c = 4.5$, which located at the downstream of the central of the second row of cooling holes, and the second row of cooling holes are interlace with the first row cooling holes, thus, the peak location of the curve of the η value is different than the curves of $Z/D_c = 1.5$. From $Z/D_c = 4.5$ to $Z/D_c = 9$, the minimum η value of this curve is not less than 0.2 (at the region between two neighboring cooling holes) due to the effect of the cooling stream from the first row of cooling holes. The overall variances between the maxima and minima are moderate because the interaction between the first row and the second row of cooling holes. At $Z/D_c = 6$, since the location is further downstream from the exit of cooling-hole arrays, the cooling effect is greatly reduced due to the interaction between the cooling stream and the main hot working fluid, however, the minimum η value still greater than 0.2 in most portions of test sample. Fig. 12(b) and (c) shows the curve of η where BR = 0.9, 1.2 respectively. Generally, the results are similar to that of BR = 0.6, but the peak value in η seems reduced with increasing of blowing ratio in regimes of $1.5 < Z/D_c < 6$. An obvious reduction in η can be observed at BR = 1.2 which indicated the occurrence of lift-off of coolant jets.

Fig. 13(a)–(c) show the lateral curve of η under different Z/D_c and blowing ratio for the FDSA cooling holes. While Fig. 14(a)–(c) show the same for the LDSA cooling holes. The curve of FDSA cooling holes similar to that in CYSA, where the major difference is at $Z/D_c = 1.5$, 4.5 where the maximum value for both the curves are greater than that of CYSA. The difference is even greater when the blowing ratio is increased. The expanding angle at the exit of the cooling holes will cause the cooling stream remain attaching on the wall by reducing the momentum with greater cross-section area and avoid the stream from lift-off. The trends from Fig. 14 are greatly different from Figs. 12 and 13. In the region between two rows of staggered cooling holes, at $Z/D_c = 1.5$, the lateral diffusion effect of the expanding hole in LDSA gives a very good protection for the area between two neighboring cooling holes. The distributions of η curves at $Z/D_c = 4.5$ and 6 are inevitably smoother than those of Figs. 12(a) and 13(a). Finally, the curve at $Z/D_c = 6$ shows the least difference between the maxima and minima, which also indicate the cooling flow give a more even protection to the flat plate. Fig. 14(b) and (c) shows the results when blowing ratio is equal to 0.9 and 1.2 respectively. The trends are similar to that of Fig. 14(a) and η value increases with the increasing of blowing ratio.

7.5. Characteristic of the flow field

Walters and Leylek [25] stated that the film cooling effectiveness over the surface are controlled by two primary mechanisms. The first is concerned with the jetting flow structure within the film hole itself. The second mechanism is due to the interaction of individual coolant jet and the cross-mainstream. Pairs of counter-rotating vortex dominate the developing of thermal-flow structure over the surface of discrete-hole film cooling plate. When the blowing ratio is equal to 1.2, Figs. 15 and 16 respectively show the velocity contour plot of H3 tube at centerline cross-plane and exit plane of coolant jets for CYSA, FDSA, and LDSA types of holes. When the cooling streams pass through the impingement pipes and flow into the cooling pipe, inspection in Fig. 15 reveals that part of cooling

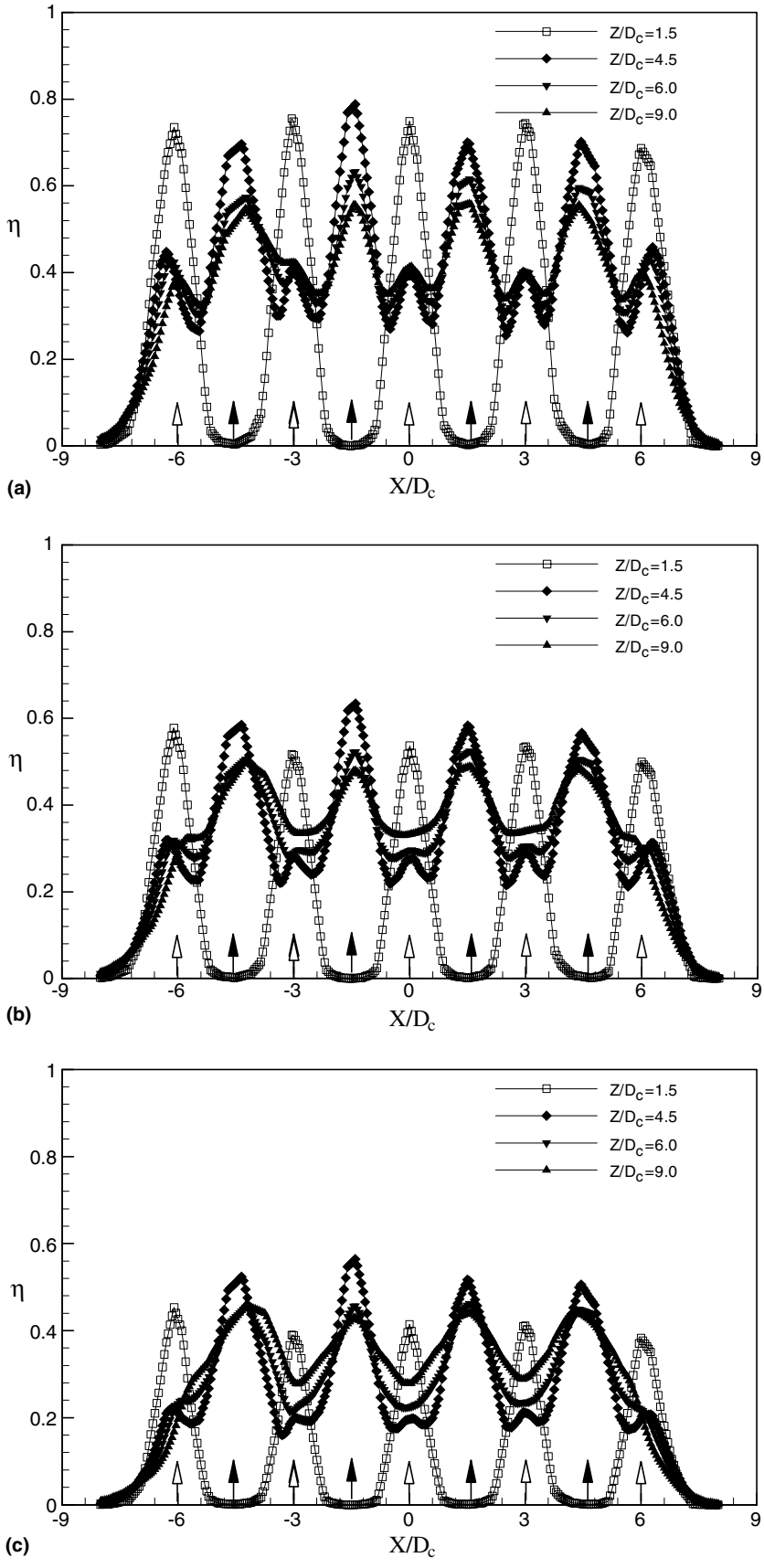

Fig. 12. Lateral distributions of local film cooling effectiveness for CYSA hole shape: (a) BR = 0.6, (b) BR = 0.9 and (c) BR = 1.2.

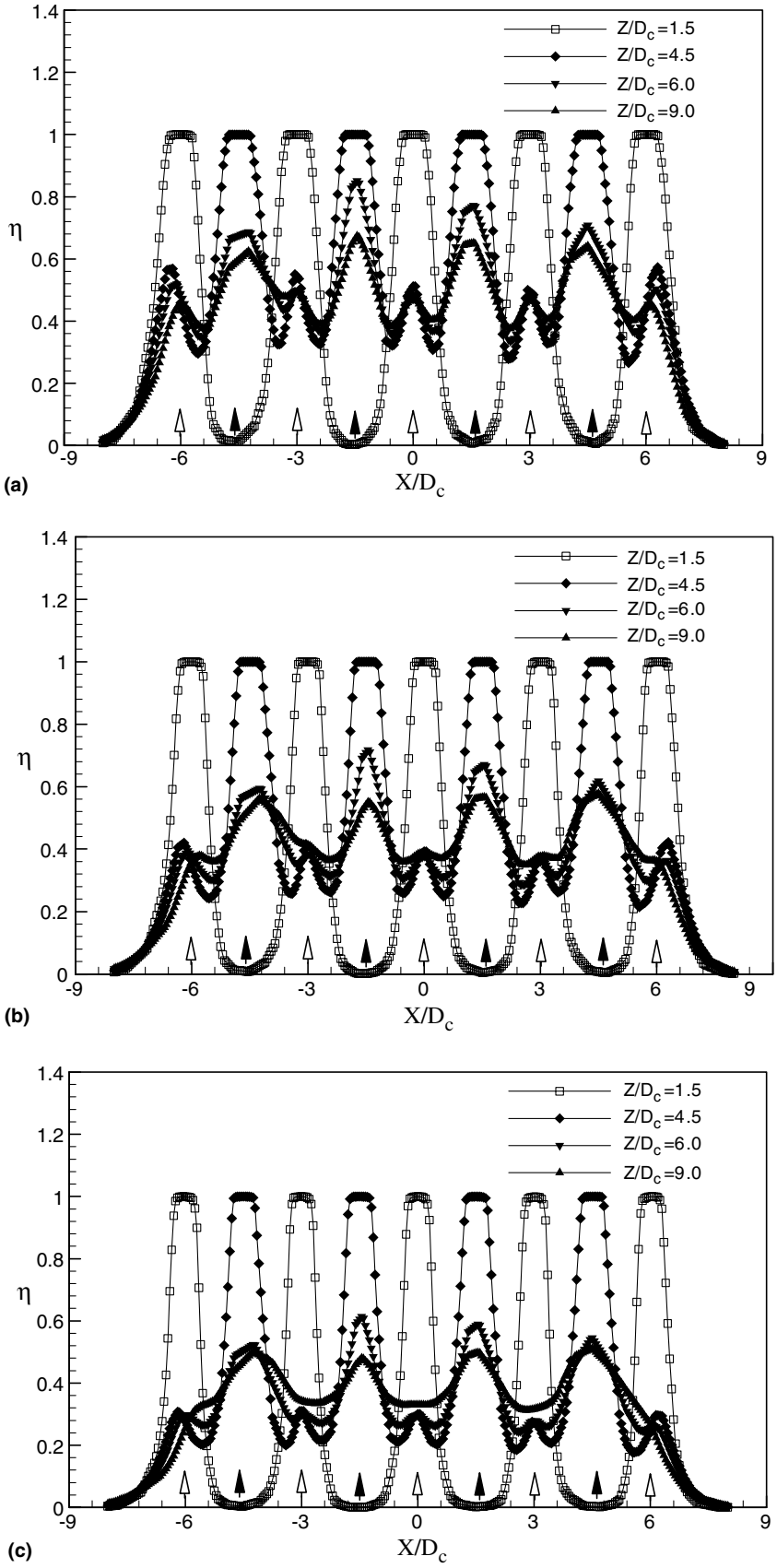

Fig. 13. Lateral distributions of local film cooling effectiveness for FDSA hole shape: (a) BR = 0.6, (b) BR = 0.9 and (c) BR = 1.2.

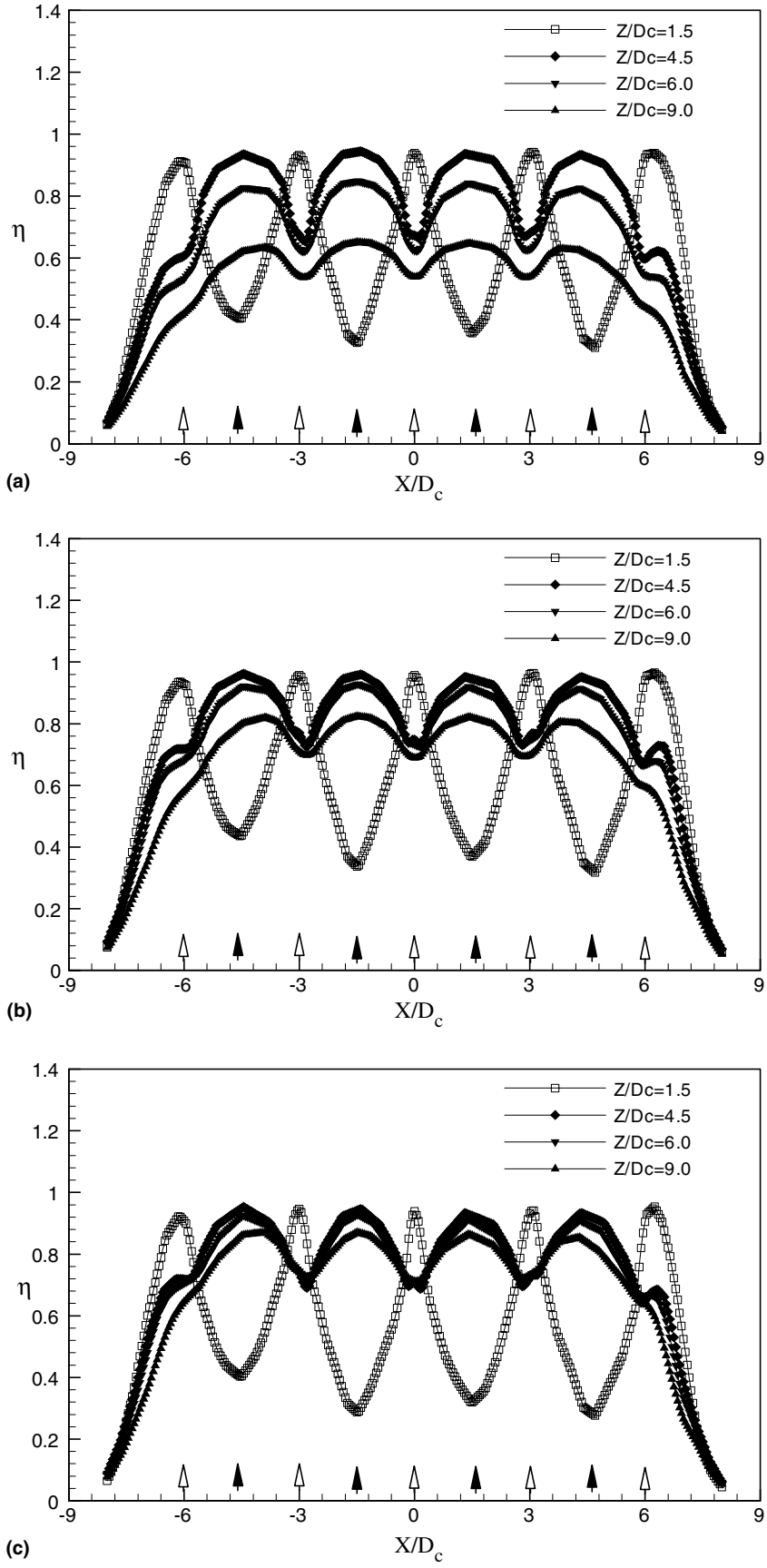

Fig. 14. Lateral distributions of local film cooling effectiveness for LDSA hole shape: (a) BR = 0.6, (b) BR = 0.9 and (c) BR = 1.2.

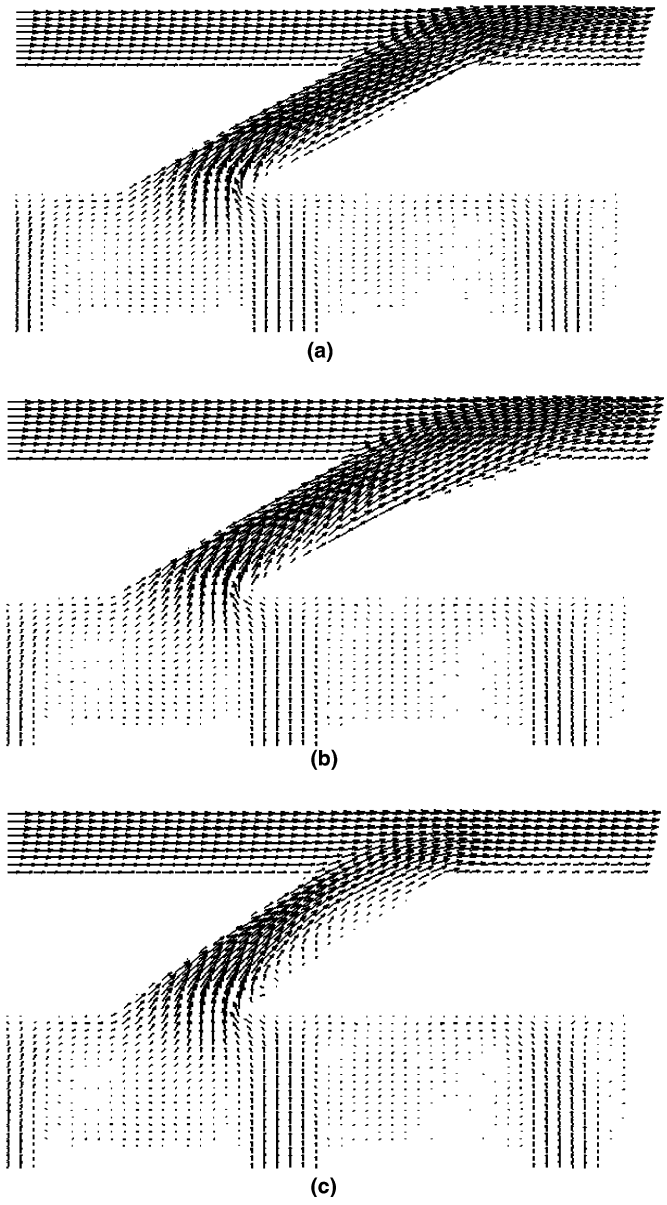

Fig. 15. Velocity vectors at central plane of H3 tube for different shapes of hole at BR = 1.2: (a) CYSA, (b) FDSA and (c) LDSA.

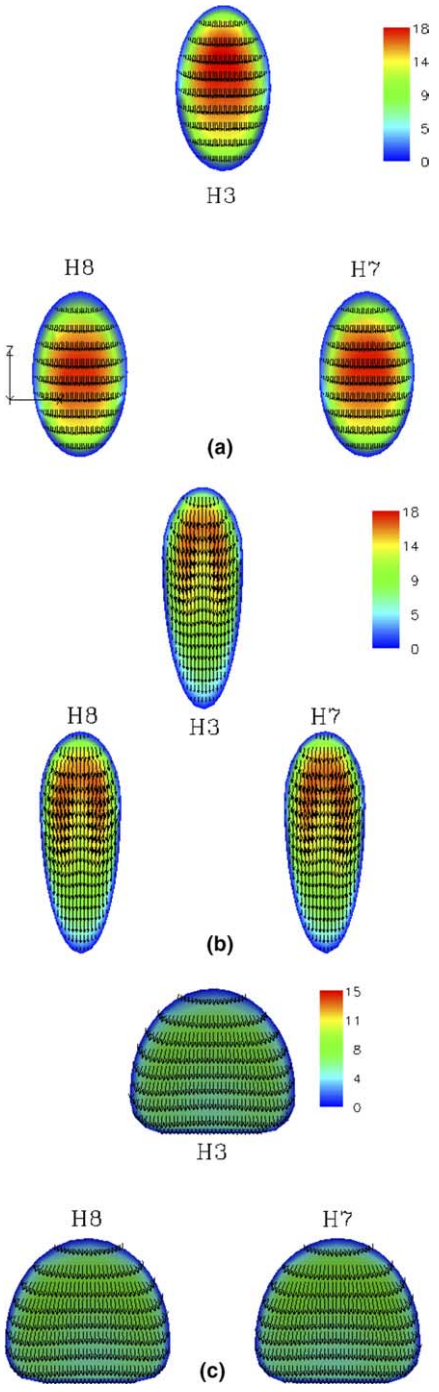

Fig. 16. Contour plots of local velocity at exit plan of coolant jets for different hole shapes at BR = 1.2: (a) CYSA, (b) FDSA and (c) LDSA.

streams may encounter a larger turning angle near the leeward side of cooling hole in lower section. Moreover, the cooling stream would pass more smoothly into the windward side of cooling hole. A major feature of "jetting flow" which is caused by the non-uniform velocity distribution at the entrance of cooling hole could display from present numerical results.

Generally, the structure of the flow field at the lower part of the cooling pipe displays with uneven fork in the curl region, which shows a higher momentum at the leeward slope but shows a lower momentum at the windward slope at tested range of blowing ratio. That is, the four parts of jetting flow, i.e. the separated/back flow area near the cooling hole entrance, the re-attachment area, developing area and the area at the tail end downstream near the cooling hole which affected by the main stream can be demonstrated from the velocity contours. In addition, a highly shear layer downstream of jet exit produced by the cooling stream penetrating into the mainstream can be observed which will cause the local film cooling effectiveness to be reduced rapidly at the near-field of jet–cross-flow intersection (Fig. 16(a)). Figs. 15(b), 16(b), 15(c) and 16(c) are the results from FDSA and LDSA types of hole, respectively. The forward-expanded structure of hole can effectively

moderate the degree of lift-off phenomena occurs in a high momentum-cooling stream. When configure of the holes are replaced by a LDSA type of hole, the lateral expanded hole will increase the cross-section of the exit and perform a lateral spreading effect. Thus, characteristics of the flow fields for CYSA and FDSA are quite different. Figs. 15(c) and 16(c) have clearly show the location that show a high momentum cooling stream is focused on the half way to the exit of the pipe instead of the region closer to the exit of the hole, where each cooling streams are interacting evenly with the mainstream and given a highest local film cooling effectiveness.

Downstream of two rows of staggered holes at cross-stream plane $Z/D_c = 6$, Fig. 17(a)–(c) shows the velocity vector for CYSA, FDSA and LDSA respectively when the blowing ratio is equal to 0.9. The counter-rotating vortex pairs generate by the cooling stream ejected from the second row of cooling holes H6–H9 can be observed clearly from Fig. 17(a) and (b). The expanding angle at the exit of FDSA has resulted in a closer attach of the vortex to the wall of the sample. This also indicates that the expanding angle can effectively reduce the lift-off of the jet from a cylindrical hole under high blowing ratio. Fig. 17(c) shows a lateral expanded angle of the LDSA type of hole that can avoid the formation of CRVP. Since the high temperature mainstream will impact on the wall due to the downwash effect of CRVP and breakup the complete and equilibrate development of the cooling film, LDSA shows the best performance in high blowing ratio (Fig. 20(c)).

7.6. Distribution of the spanwise-averaged film cooling effectiveness

The effect of internal impingement flow on the streamwise distributions of spanwise-averaged η value for CYSA hole at various blowing ratios are observed in Fig. 18. For cases with or without the impingement pipe array, the effect of blowing ratio on the $\bar{\eta}$ distributions is quite similar. In regions of $0 < Z/D_c < 15$, the highest $\bar{\eta}$ value occurs for cases of BR = 0.6 for both runs. At the same blowing ratio, it seems that the arrangement of present internal impingement pipe array enhances the $\bar{\eta}$ value for most portions of tested plate. This is due to the impingement tubes are located just beneath on the coolant pipes; the less degree of jetting flow developing in coolant tube prevents the penetration of coolant flow.

Fig. 19(a)–(c) shows the effect of blowing ratio on the spanwise-averaged film cooling effectiveness along the streamline for CYSA, FDSA and LDSA, respectively. The two peaks value of the distribution of the curve are

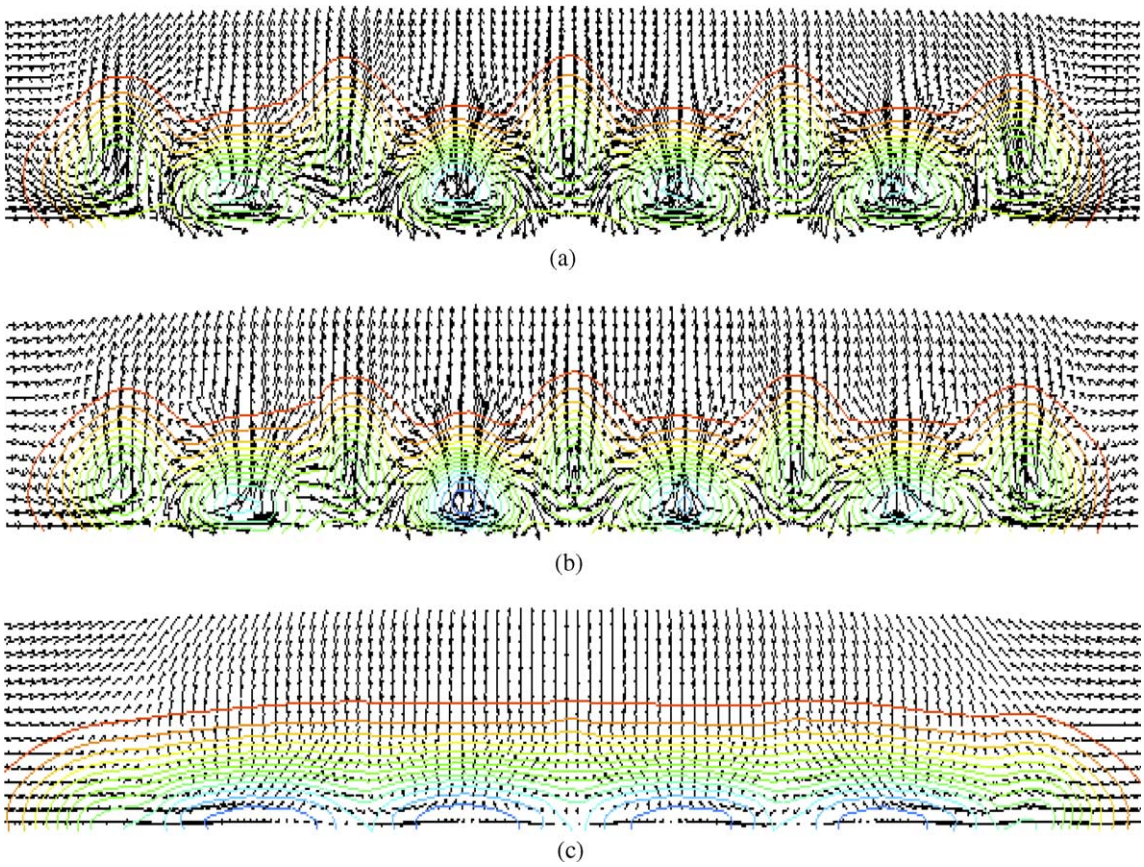

Fig. 17. Velocity vectors in the spanwise plane at $Z/D_c = 6$ for different hole shapes at BR = 0.9: (a) CYSA, (b) FDSA and (c) CDSA.

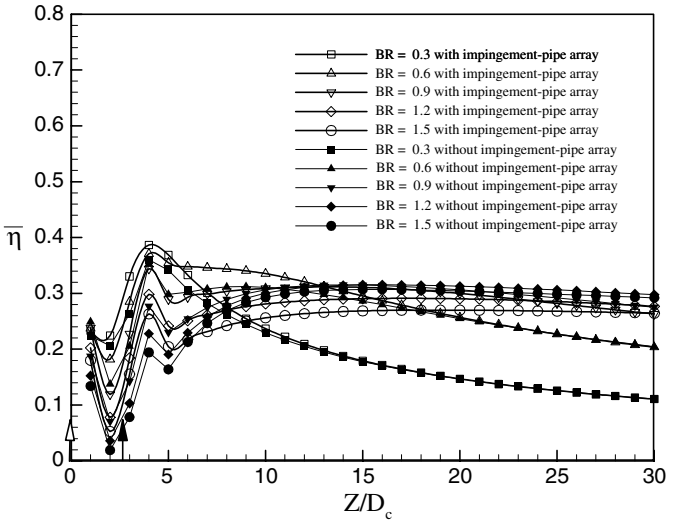

Fig. 18. Streamwise distributions of spanwise-averaged film cooling effectiveness for CYSA hole with and without internal impingement pipe array at various blowing ratios.

caused by the cooling stream ejected from holes belong to the first and the second row. The highest $\bar{\eta}$ value for holes of CYSA and FDSA occurs for blowing ratio of 0.6. As the blowing ratio is above 0.9, both shapes of hole could not prevent the penetration of coolant jets into the cross-hot mainstream. Therefore, the decreasing in $\bar{\eta}$ values with increasing of blowing ratio can be clearly observed. At the downstream of injection holes, the spanwise-averaged film cooling effectiveness of LDSA hole will increase with respect to the blowing ratio. Moreover, the lowest value of $\bar{\eta}$ at $0 < Z/D_c < 3$ for a CYSA hole can be drastically increased by applying FDSA or LDSA type of holes. The effect of different types of cooling holes can be observed from Fig. 20(a) under fixed blowing ratio of BR = 0.6. In the near-field jet–cross-flow region of $Z/D_c \leqslant 10$, a visible difference in spanwise-averaged film cooling effectiveness for different shape of hole is existed. At $Z/D_c = 1$ and 4, i.e. locates next to the downstream of the cooling hole, LDSA gives the highest value of $\bar{\eta}$, then CYSA, while FDSA type of hole shows the lowest value. At $Z/D_c = 2$, LDSA still gives the highest value of $\bar{\eta}$, then FDSA, and CYSA type of hole shows the lowest value. The distribution of $\bar{\eta}$ for the three types of holes are very close to each other downstream of $Z/D_c = 20$. The LDSA structure still exhibits the highest spanwise-averaged film cooling effectiveness when the blowing ratio is 0.9, shown in Fig. 20(b). The $\bar{\eta}$ value for FDSA is higher than that of CYSA downstream of cooling holes. When the blowing ratio further increases to 1.2, Fig. 20(c) shows that the $\bar{\eta}$ value of LDSA structure in region of $0 \leqslant Z/D_c \leqslant 30$ is the highest among the three types of holes, while CYSA shows the lowest value of all. We can also discover that the $\bar{\eta}$ values do not change much for FDSA and CYSA

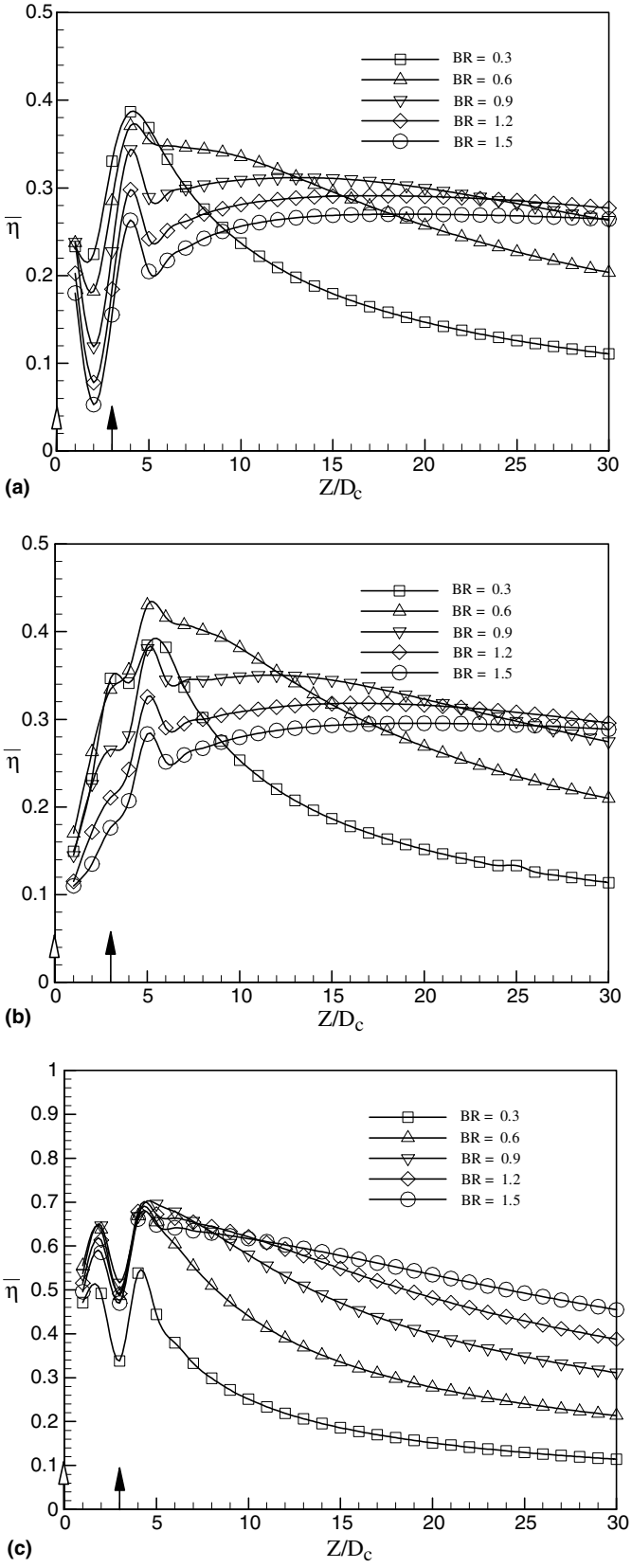

Fig. 19. Streamwise distributions of spanwise-averaged film cooling effectiveness at various blowing ratios: (a) CYSA, (b)FDSA and (c)LDSA.

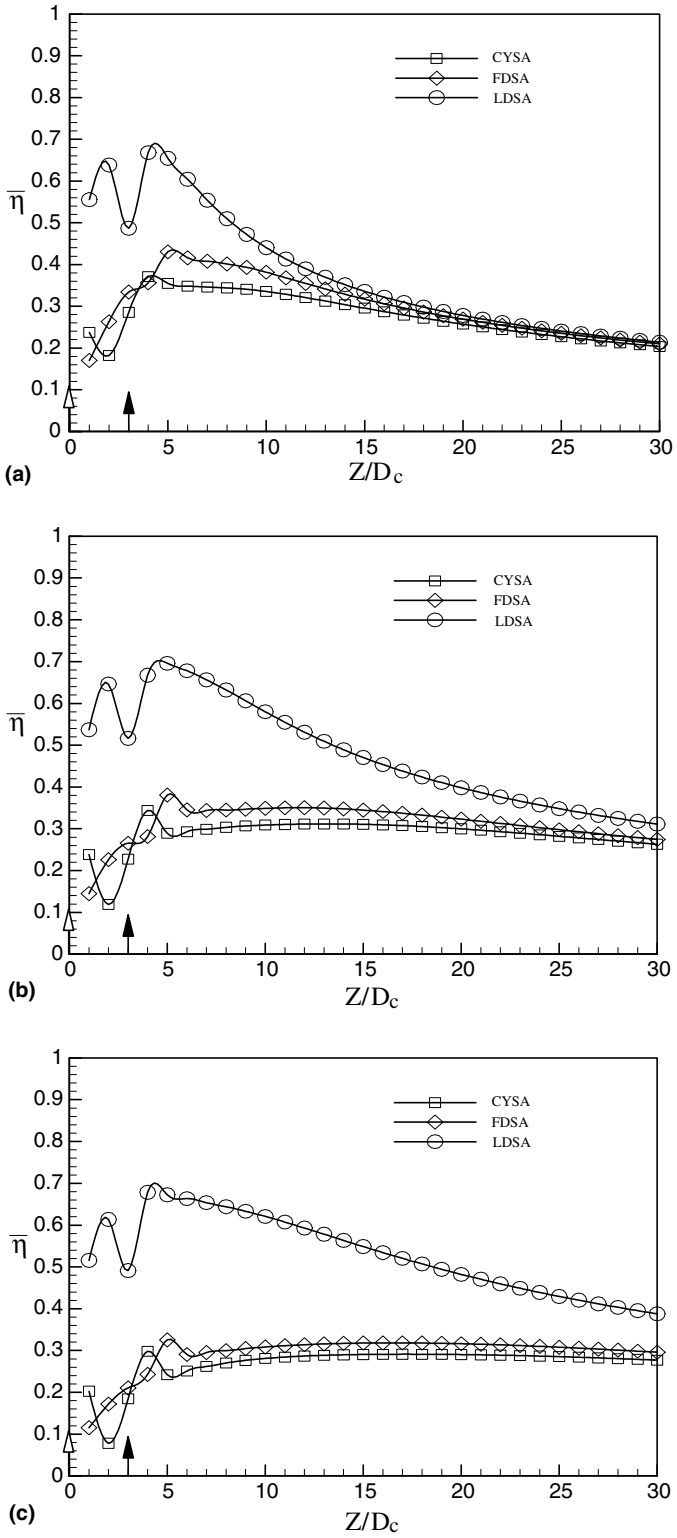

Fig. 20. Streamwise distributions of spanwise-averaged film cooling effectiveness for different hole shapes: (a) BR = 0.6, (b) BR = 0.9 and (c) BR = 1.2.

when the blowing ratio above 0.9 by comparing Fig. 20(b) and (c).

8. Conclusion

This paper has performed a systematic numerical simulations on the characteristic of the 3-D thermal-flow field of an impinging cooling/film cooling dual effect sample flat plate with different kinds of hole shapes under five blowing ratios (BR = 0.3, 0.6, 0.9, 1.2 and 1.5). The cooling holes are distributed in two rows that interlace between each other in pitch of three times of diameter of hole. The types of holes being used in the study are: cylindrical round, simple angle hole (CYSA), forward diffused, simple angle hole (FDSA) and lateral diffused, simple angle hole (LDSA). Some major numerical simulation conclusions are as below:

(1) The present paper accomplished a realistic cooling study on turbine blade with numerical approach. The tested sample is a film-cooled flat plate with internal impingement cooling chamber. Using ICEM/CFD as the preprocessor, the multi-block and body-fitted computational grid system that includes the mainstream duct, two rows of cooling pipes, impingement chamber, and supply plenum regions are constructed successfully.
(2) The simulated velocity contours clearly displayed that the structure of the flow field within cooling hole tube can be separated as the windward high momentum area at the entrance, the contrariwise low momentum at split of the curl, central developing area and the exit region that directly affected by the mainstream. The structure of jetting flow is under the influence of both geometrical shape of hole and blowing ratio. Further, CRVP is observed clearly in both of CYSA and FDSA. Simulated results also exhibit that CRVP does not exist in LDSA hole, especially for high blowing ratios. Thus, LDSA provides better protection on sample surface.
(3) The geometrical shape of cooling hole plays a significant effect to the adiabatic film cooling effectiveness. Near-field of jet–cross-flow intersection, LDSA hole would give a better later coverage of the cooling stream on the surface of the sample flat plate as expected.
(4) The lift-off phenomena of coolant jets occur for CYSA at blowing ratio of 0.9. Although the FDSA hole can enhance the overall $\bar{\eta}$ value, the lift-off phenomena still exist when the blowing is above 0.9. As blowing ratio increasing from 0.3 to 1.5, the LDSA has shown a better cooling performance than other shapes. It is due to the structure of the LDSA can reduce the momentum of the cooling flow at trailing edge of cooling holes, thus reduced the streamwise penetration of the mainstream. Moreover, the structure of the LDSA can increase the lateral spread of the cooling flow, thus improves the spanwise-averaged film cooling effectiveness.

(5) In the tested range of blowing ratios, present results for CYSA holes indicate that the arrangement of internal impingement pipe array can enhance the $\bar{\eta}$ value for most portions of tested plate.

Acknowledgement

This finical support from NSC under contract number of NSC 90-2212-E-014-018 is deeply appreciated.

References

[1] J.-C. Han, S. Dutta, S. Ekkad, Gas Turbine Heat Transfer and Cooling Technology, first ed., Taylor & Francis, New York, 2000, Chapter 4, p. 252.
[2] H.D. Ammari, N. Hay, D. Lampard, The effect of density ratio on the heat transfer coefficient from a film-cooled flat plate, ASME J. Turbomach. 112 (1990) 444–450.
[3] R.J. Goldstein, P. Jin, R.L. Olson, Film cooling effectiveness and mass/heat transfer coefficient downstream of one row of discrete holes, ASME J. Turbomach. 121 (1999) 225–232.
[4] S. Baldauf, A. Schulz, S. Wittig, High-resolution measurements of local heat transfer coefficients from discrete hole film cooling, ASME J. Turbomach. 123 (2001) 749–757.
[5] S. Baldauf, A. Schulz, S. Wittig, High-resolution measurements of local effectiveness from discrete hole film cooling, ASME J. Turbomach. 123 (2001) 758–765.
[6] P.J. Loftus, T.V. Jones, The effect of temperature ratios on the film cooling process, ASME J. Eng. Power 105 (1983) 615–621.
[7] P.M. Ligrani, A. Ortiz, S.L. Joseph, D.L. Evans, Effects of embedded vortices on film-cooled turbulent boundary layers, ASME J. Turbomach. 111 (1989) 71–77.
[8] H.H. Cho, R.J. Goldstein, Heat (mass) transfer and film cooling effectiveness with injection through discrete holes: Part I—Within holes and on the back surface, ASME J. Turbomach. 117 (1995) 440–450.
[9] J.H. Leylek, R.D. Zerkle, Discrete-jet film cooling: a comparison of computational results with experiments, J. Turbomach. 116 (1994) 358–368.
[10] D.G. Hyams, J.A. Leylek, A detailed analysis of film cooling physics. Part III: Streamwise injection with shaped holes, ASME J. Turbomach. 122 (2000) 122–132.
[11] C.M. Bell, H. Hamakawa, P.M. Ligrani, Film cooling from shaped holes, ASME J. Heat Transfer 122 (2000) 224–232.
[12] M. Gritsch, A. Schulz, S. Wittig, Film-cooling holes with expanded exits: near-hole heat transfer coefficients, Int. J. Heat Fluid Flow 21 (2000) 146–155.
[13] I.S. Jung, J.S. Lee, Effects of orientation angles on film cooling over a flat plate: boundary layer temperature distributions and adiabatic film cooling effectiveness, ASME J. Turbomach. 122 (2000) 153–160.
[14] Y. Yu, C.H. Yen, T.I.P. Shih, M.K. Chyu, S. Gogineni, Film cooling effectiveness and heat transfer coefficient distributions around diffusion shaped holes, ASME J. Turbomach. 124 (2002) 820–827.
[15] A.I. Behbahani, R.J. Goldstein, Local heat transfer to staggered arrays of impingement circular air jets, ASME J. Eng. Power 105 (1983) 354–360.
[16] Y. Huang, S.V. Ekkad, J.-C. Han, Detailed heat transfer distributions under an array of orthogonal impinging jets, J. Thermophys. Heat Transfer 12 (1998) 73–79.
[17] G.S. Azad, Y. Huang, J.-C. Han, Impingement heat transfer on dimpled surfaces using a transient liquid crystal technique, J. Thermophys. Heat Transfer 14 (2000) 186–193.
[18] S.J. Downs, E.H. James, Jet impingement heat transfer-a literature survey, ASME Paper 87-HT-35, 1987.
[19] R. Viskanta, Heat transfer to impingement isothermal gas and flame jets, Exp. Thermal Fluid Sci. 6 (1993) 113–134.
[20] H.H. Cho, D.H. Rhee, B.G. Kim, Enhancement of film cooling performance using a shaped film cooling hole with compound angle injection, JSME Int. J. Ser. B 44 (1) (2001) 99–110.
[21] R. Schiele, S. Wittig, Gas turbine heat transfer: past and future challenges, J. Propulsion Power 16 (4) (2000) 583–589.
[22] D. Ai, P.P. Ding, P.H. Chen, The selection criterion of injection temperature pair for transient liquid crystal, Int. J. Heat Mass Transfer 44 (2001) 1389–1399.
[23] D.C. Wilcox, Turbulence Modeling for CFD, DCW Industries Inc, La Canada, CA, 1993.
[24] H. Nasir, S.V. Ekkad, S. Acharya, Effect of compound angle injection on flat surface film cooling with large streamwise injection angle, Proceeding of the 8th International Symposium on Transport Phenomena and Dynamics of Rotating Machinery 2 (2000) 763–768.
[25] D.K. Walters, J.H. Leylek, A detailed analysis of film-cooling physics. Part I—Streamwise injection with cylindrical holes, ASME J. Turbomach. 122 (2000) 102–112.